



Process window and mechanical properties for thin magnesium- and zinc-wires in dieless wire drawing

Merle Braatz¹ · Jan Bohlen¹ · Noomane Ben Khalifa^{1,2}

Received: 22 May 2024 / Accepted: 1 July 2024 / Published online: 12 July 2024
© The Author(s) 2024

Abstract

Due to their biodegradable properties, magnesium- and zinc-based alloys are in the focus of interest for numerous medical applications, e.g. in the form of thin wires. To achieve improved processability by using hot forming and to obtain higher diameter reductions per pass, the dieless wire drawing process is presented in this paper. In order to investigate the processability and the resulting mechanical properties, a selection of magnesium- and zinc-alloys as well as process parameters are chosen, and wire manufacturing is carried out using the dieless drawing process. The resulting process windows and mechanical properties for the selected materials are discussed. It is found that the length of the forming zone is an important indicator for the process window and the cross-sectional area reduction accuracy in the dieless wire drawing process. Furthermore, process parameter variations result in a distinct variation of the mechanical properties of the wires, whereas process temperatures close to the wire extrusion temperature result in mechanical properties similar to the as-extruded wires. Good localization of the deformation is found for forming zones of 25–75 mm length at elevated temperatures and cross-sectional area reductions of up to 30% are possible for Z1 and ZX10 in one drawing step.

Keywords Dieless wire drawing · Magnesium · Zinc · Process window · Property development

Introduction

In the presented dieless wire drawing (DD) process (see Fig. 1), the wire moves with a feeding speed v_0 and a higher drawing speed v_1 , while an induction coil heats the wire locally, thus creating a heating zone. While moving forward, the wire is then passively cooled by air after leaving the heated zone. When the flow stress of the material has been sufficiently reduced by the temperature applied, the deformation of the material (forming zone) begins at the point of lowest flow stress at maximum temperature, which is reached when the material exits the induction coil [1]. In combination of this localized plastic deformation zone and the globally applied tensile load F (resulting from the

speed ratio v_0/v_1), the diameter reduction of the wire from the initial cross-sectional area (CSA) A_0 to the final CSA A_1 is initiated kinematically. With an adjustable drawing force, the process can achieve large CSA reductions in a single pass, making it a more efficient hot manufacturing process for manufacturing thin wires.

The overall degree of deformation for the DD process is given by:

$$\varphi = \ln \left(\frac{A_0}{A_1} \right). \quad (1)$$

Together with the equation for volume constancy which applies for the DD process.

$$v_0 * A_0 = v_1 * A_1, \quad (2)$$

the deformation equation (Eq. 1) can also be written as:

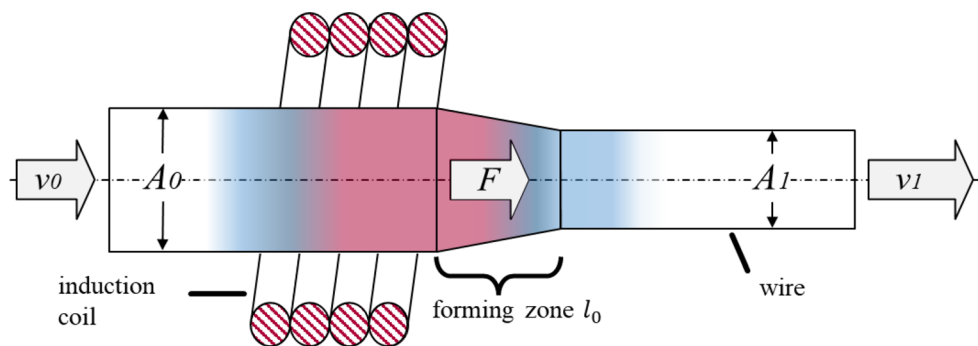
$$\varphi = \ln \left(\frac{v_1}{v_0} \right). \quad (3)$$

✉ Merle Braatz
merle.braatz@hereon.de

¹ Institute of Material and Process Design, Helmholtz-Zentrum Hereon, Max-Planck-Straße 1, 21502 Geesthacht, Germany

² Institute for Production Technology and Systems, Leuphana Universität Lüneburg, Universitätsallee 1, 21335 Lüneburg, Germany

Fig. 1 Schematic illustration of the DD process



The CSA reduction R of the wire before and after the DD process can then be determined as [2]:

$$R = 1 - \frac{v_0}{v_1} = 1 - \frac{A_1}{A_0} \tag{4}$$

Since the CSA reduction R can be determined by the set process speeds and by the wire diameters before and after the DD process, it is proposed to distinguish between the analytical CSA reduction R_{an} and the experimental CSA reduction R_{exp} :

$$\text{Analytical : } R_{an} = 1 - \frac{v_0}{v_1} \tag{5}$$

$$\text{Experimental : } R_{exp} = 1 - \frac{A_1}{A_0} \tag{6}$$

The DD process was first introduced in 1969 by Weiss and Kot [3] and experimentally analysed in 1975 by Sekiguchi and Kobatake [4]. Even though the DD process is not new, the technique is still one of the newest methods of innovative forming in wire drawing and has not been industrialised yet [5]. Mainly because the drawing speed in industrialised conventional wire drawing is significantly higher than in the DD process [6] and it only seemed profitable for special applications like tapered-rod coil springs [7]. However, over the last 20 years, DD has increasingly been the focus of studies to improve productivity and cost-effectiveness [8], as well as of medical engineering interests [9]. The DD process has the advantage of contactlessness, i.e. no tooling or lubricant affect the surface and the material itself. It also is a self-initiating hot forming process which, due to its characteristics, enables the development of properties that can be achieved by solid forming processes.

Early studies deal mostly with the feasibility and the description of the process itself: Tiernan and Hillery [10] describe the sensitivity of the DD process to its parameter settings and the existence of a non-stable phase at the beginning of the process with a following steady-state [11]. Naughton and Tiernan [5] analyse the process stability for

wires and Milenin et al. [12] for microtubes. The feasibility of the process applied to Mg-based alloys is described by Furushima and Manabe [13] for microtubes and by Milenin et al. [14] for wires. First studies also show the feasibility of producing Zn-based microtubes [15] and thin Mg and Zn wires [1].

A feasible DD process setup and its process stability depend on whether the process steady-state is reached or not for a given set of processing parameters. The independent and controllable parameters of the DD process are the properties of the used material (especially temperature and strain rate dependent material behaviour; by material change or alloying), the process temperature and the process feeding and drawing speed. A change in the speed ratio v_0/v_1 changes the resulting drawing force, which influences mechanical parameters like strain, strain rate and stress. A change in the process temperature influences material parameters like the flow stress and therefore kinematic and mechanical parameters again. The independent DD parameters temperature and speeds can thus be described by equations for heat transfer and strain coupled in both directions. Of these independent parameters, the temperature is the main control parameter because it can be influenced locally by heating and (active) cooling, whereas the speed ratio v_0/v_1 can only be controlled globally.

To understand the process parameters, Fortunier et al. [16] first and later Pawelski and Kolling [17] describe the temperature profile and Weidig and Steinhoff [18] first define a forming zone during the DD process for steel wires. In order to describe the thermo-mechanical coupling effect and thus investigate the influencing process parameters, Wengenroth et al. [19] couple a heat conduction equation and a balance of stresses to the result in:

$$\frac{dr}{dx} = -\frac{r^3}{2v_0r_0^2} \left\{ \frac{\sigma \exp(m_1T)}{C(\phi + \phi_0)^{m_2} \exp[m_4/(\phi + \phi_0)]} \right\}^{1/m_3} \tag{7}$$

With σ and ϕ representing stress and strain, T being the temperature, x the wire longitudinal position, r the wire radius, v the process speed and $C, m_1 \dots m_4$ being material constants. Index 0 represents the parameter in the initial

process condition. This equation shows that the change in radius of the wire over its length depends on several factors. The first multiplier describes a basic dependence of the diameter profile on the initial diameter and the feeding speed. The second part of the equation basically describes the exponential dependence of the temperature and strain rate and material dependent behaviour, which influence each other. Taking (Eq. 7), the diameter reduction profile of the DD wire is therefore based on interactions between the parameters process speed, process temperature, process stress, and the thermomechanical properties of the used material. Based on an instability criterion, He et al. [20] first introduce a processing limit map through a stability criterion that detects unstable deformation consisting of wire fracture and diameter variations for tin bronze wires in DD. And Hwang et al. [21] investigate forming limits and dynamic recrystallization for titanium wires. Studies of property development for DD are mostly done for steel wires (e.g. [22]) and for Mg-based wires only for AZ31 wires [23], other materials (e.g. brass [24] or titanium [25]) or for microtubes [26, 27]. For Zn-alloys, wire properties are only investigated for conventional drawing [28] or are compared for conventional warm and cold drawing processes [29]. However, further systematic approaches to investigate the process window of DD wire drawing and studies for Mg- and Zn-based wires are not available in the present literature.

Due to their biodegradable and non-toxic properties, Magnesium (Mg)-based and Zinc (Zn)-based wires are used in medical engineering e.g., for suture [30] or as stent solutions [31] and they have excellent specific strength and stiffness for a number of applications. Unlike Mg-based wires, Zn-based wires have a slower corrosion rates in urine [32] and blood [33] related environments, making Mg-based wires suitable for shorter-term and Zn-based wires for longer-term biomedical applications. However, for Mg- and Zn-alloys the low technological plasticity which is connected with their characteristic closed-packed lattice structure also results in a rather low ductility and low formability of the material at room temperature [34]. The hexagonal lattice structure influences the forming of Mg so that reductions in CSA of more than 10% (or 15% with lubricants [35]) in a single wire drawing pass at room temperature are critical and mostly result in fracture of the wires [6]. Nienaber et al. [36] show that the alloying of Mg can improve the formability in wire drawing up to a CSA reduction of 20% in classical cold wire drawing when combined with intermediate heat treatments. To achieve higher overall reduction in CSA, multiple die drawing passes with intermediate heat treatments are widely used, where the heat treatment contributes to the required material softening and therefore the recovery of its initial ductility. To use these effects and improve material flow during the forming, forming processes at elevated

temperatures are used. This allows the use of specialised hot forming process such as DD for the drawing of thin Mg- and Zn-based wires, which uses contactless thinning based on localised heating and therefore localised deformation of the wires during processing.

But reducing the diameter is only possible if the chosen parameter settings are applicable and the DD process has reached its steady-state. Thereby, the feasibility and accuracy of the DD process are dependent on the material response to the process parameters (temperature and speeds) and thus on the development of a forming zone when the steady-state of the process is reached. In earlier work in Braatz et al. [1], the forming zone in the DD process and the influence on its length and therefore on the process stability are investigated. If there is no successful transition into the steady-state, the process parameter settings are not applicable and result in the fracture of the wire. Thus, the establishment of the steady-state condition along the development of the forming zone is an important process-related indicator for the process window. For this reason, the length of the forming zone is an important indicator for the process window and the accuracy of the DD process. For this paper, the process windows for selected Mg- and Zn-alloys are determined, and the resulting mechanical properties are discussed for the DD process.

Materials and methods

Materials

Investigations towards biodegradable metallic materials focus on both, Mg and Zn. However, pure Mg and pure Zn do not offer a favoured property profiles in terms of corrosion rate and formability [37]. Alloying elements can influence the microstructure and favour thermomechanical homogenisation. For example adding Calcium (Ca) and Zn to pure Mg or Copper (Cu) to pure Zn is an effective means of improving the mechanical strength and the corrosion resistance [37]. In Mg-alloys, Ca contributes to an improved formability alongside with grain refinement [38] and it reduces the corrosion rates if the Ca content is below 1 wt%. During hot working, Zn in Mg-alloys accelerates recrystallisation and can lead to grain coarsening [39]. The tensile properties and corrosion rates of binary Mg–Zn alloys strongly depended on the Zn content and the existence of secondary phases [40]. Thus, for a good combination of mechanical properties and corrosion resistance, Zn should be limited to max. 4 wt% [41]. In the ternary Mg–Zn–Ca alloy system, a Ca content of less than 0.5 wt% at 1 wt% Zn shows a significant reduction of the corrosion rate compared to the binary Mg–Ca system [42], while larger amounts of

Table 1 Extrusion parameters for used Mg- and Zn-alloys

Feedstock material	Extrusion temperature in °C	Ram speed in mm/s
Z1 (Mg-1%Zn)	350	0.2
ZX10 (Mg-1%Zn-0.15%Ca)	400	0.2
ZnCu (Zn-2%Cu)	250	0.1

Ca or Zn again lead to an increase in corrosion rates [43]. For the Zn-alloy, the addition of Cu shows satisfying long-term mechanical properties in Hank's solution tests and additionally, Zn-2%Cu and Zn-3%Cu alloys indicate good antibacterial activity [44]. While higher Cu contents further increase mechanical properties, it also increases the corrosion rate [45] and therefore the amount of added Cu should be limited. Based on the above, potential biometallic alloy solutions Z1 (Mg-1%Zn), ZX10 (Mg-1%Zn-0.15%Ca), and Zn-2%Cu were chosen in the framework of this study.

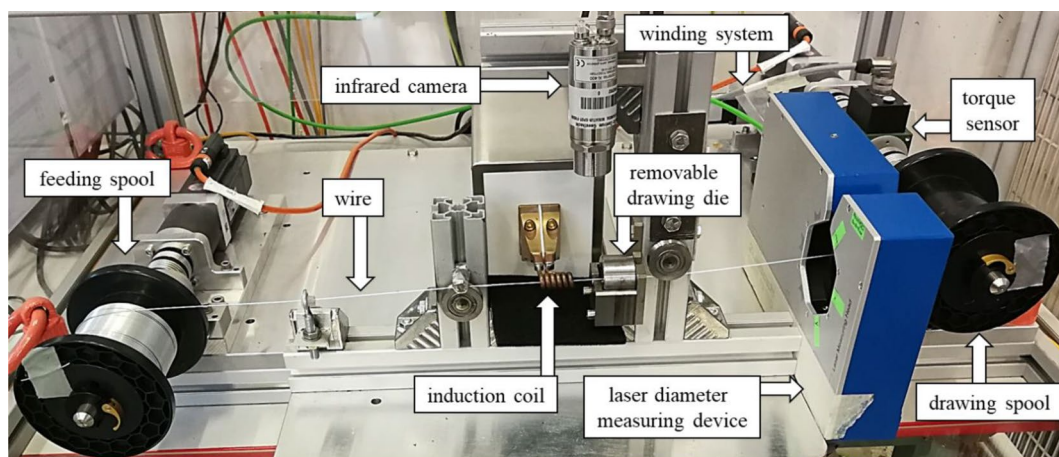
Directly extruded wires with 1 mm diameter of alloys Z1, ZX10, and ZnCu are used as feedstock materials for the DD experiments. The alloys are cast into ingots and are then machined into cylindrical shape. A direct extrusion process at elevated temperatures is applied using a die with four 1 mm diameter nozzles positioned equidistant from the centre. Details on the extrusion setup can be obtained from earlier work in Nienaber et al. [46] and the extrusion temperatures and ram speeds for the used alloys are listed in Table 1.

Dieless wire drawing setup

A flexible wire drawing setup is used for carrying out the DD experiments. The design of the setup is based on modularity and simplicity for DD experiments and classical wire drawing experiments with die and for a better comparison of both process variants [47]. Figure 2 shows an image of

the flexible wire drawing setup; for this study, the die next to the induction coil is removed as only DD experiments are carried out. The as-extruded wires are placed in the setup on the left-hand side, guided through the induction coil, and fixed to the right-hand wire spool. The wire receives a pre-tension of 10 N prior to the start of the experiments. The low preload is used to ensure that the wire is well positioned in the setup to avoid speed and force fluctuations due to a loose wire or process stops caused by the wire touching the induction coil, resulting in a safety shutdown of the system. After setting the feeding and the drawing speed, the power of the generator, and the process time, the process velocities and induction heating start simultaneously as well as the winding on the right-hand wire spool. In order to measure the length of the forming zone during the steady-state of the process, the drawing speed v_1 is set to the feeding speed v_0 , while the heating of the induction coil is switched off simultaneously at the end of the experiment.

For a continuous DD setup, the localized heating zone is realized using a stationary induction coil which is powered by a 2 MHz Himmelwerk high frequency generator. The high frequency generator is integrated and controlled by a real-time Profinet interface. Induction heating is applied often in DD processes because it offers fast controllability and sufficient heating rates [20]. Due to the small CSA of the wires, the process allows passive cooling at ambient air temperature. A thermal imaging Optris Xi400 infrared camera with a macro-optic is used to measure the wire temperature with an accuracy of ± 10 °C. Infrared temperature measurements are based on the emissivity of the material and its surface structure. Additionally, the emissivity of Mg changes for different temperatures (e.g. [48]). Therefore, the required emission coefficients are determined using a matt black spray paint of known emissivity to calibrate the temperature measurements. In the DD process the tensile force, leading to deformation within the heating zone, is

**Fig. 2** Flexible wire drawing setup

generated indirectly in the wire longitudinal direction [49]. In the used setup, the tensile force is applied by two servo motors which independently control the feeding and the drawing speeds v_0 and v_1 , respectively. The setup allows continuously adjustable process speeds from 1 mm/s up to 90 mm/s (up to 20 mm/s in the framework of this study), to cover lower process limits as well as possible slow- and high-speed applications [50]. On the drawing side, a torque sensor (accuracy of $\leq \pm 0.5\%$ and load capacity of max. 10 Nm) is embedded to calculate process forces and a linear laying system is installed to enable controlled winding of long wires. Additionally, a Zumbach ODAC 13TRIO laser measuring head measures the wire diameter. Due to the limited installation space and its electronics, the instrument is placed at a distance from the induction coil. The wire position of the diameter measurements is then corrected by the distance from the end of the induction coil to the laser measurement point. A Beckhoff automation solution is used for component integration, driving and control technology, and value export during process time. The process time, calculated process force, servomotor speeds and diameter measurements are exported every 0.5 s.

For a systematic approach, a parametric study is carried out with experiments at temperatures of approx. $T = 50, 150, 250, 350, 450$ °C (for ZnCu max. 400 °C because of its melting temperature) and with feeding speeds $v_0 = 5, 10, 20$ mm/s. The required drawing speeds v_1 to achieve the desired CSA reductions $R_{an} = 10, 20, 30\%$ are calculated from (Eq. 5). The resulting CSA reductions R_{exp} are calculated from (Eq. 6).

Testing methods

Tensile tests using a universal testing machine Zwick05 with a maximum load of 5 kN are carried out and are used to determine the mechanical properties of the dieless drawn wires. At least three samples of each parameter setting are tested at ambient air temperature and a constant initial strain rate of 10^{-3} s^{-1} . Strain measurements are carried out using mechanical extensometers at a gauge length of 50 mm. From the measurements, stress-strain diagrams and the related stress and strain properties are obtained.

Results and discussion

For analysing the process window, the process response within the steady-state of the DD process is important. Direct process responses are the changes in the wire diameter and in the acting tensile force. Figure 3 shows typical wire diameter evolution (in grey) and process force values (in red) along the wire position during processing for ZX10

at different temperature levels. Gaps in the line graphs are due to the spray paint used to calibrate the temperature measurement. At the beginning, the diameter reduces in a slope until the final diameter of the drawn wire is established. The distance from the last initial diameter to the first final diameter measurement is coloured yellow and marks the transition zone. During these first process seconds, the DD process transitions from a non-stable phase to its stable steady-state where the process forces, temperatures and material reactions are finally in steady-state and the forming zone is established. At the end of the experiment, the tensile force is taken out of the system and the heating is shut off. The distance from the last final diameter back to the first initial diameter measurement at the end of the wire is coloured blue and marks the forming zone length l_0 . The process force develops in a different manner. Here, for temperatures below 250 °C (Fig. 3a and b), the force increases like a saturation curve until it reaches a maximum plateau when the steady-state is reached. For higher temperatures (Fig. 3c and d), the force increases at the beginning of the process and then drops to its steady-state value because of the material response to temperature induced lower material flow stress. In both cases, the force drops when the feeding speed is set to the drawing speed for forming zone measurements at the end of the experiments.

Furthermore, at the same process speeds but at different temperatures, different process reactions can be seen in Fig. 3 with different transition and forming zone lengths. As mentioned above, the length of the forming zone is an important indicator for the process window and reduction accuracy in correlation to the chosen parameter settings in the DD process. Therefore, parameter interactions and their influence on the length of the forming zone are investigated. From (Eq. 7), the parameter interactions are analytically influenced mainly by the temperature, but also by the process initial (feeding) speed and the acting tensile stress.

Process windows

For better comparison of values, the process forces are normalized to the unknown wire diameter in the forming zone. The average flow stress σ_f is calculated using the exported force values F , the respective speeds v_0, v_1 and final wire CSA A_1 [5]:

$$\sigma_f = \frac{F(1 - \frac{v_0}{v_1})}{A_1 \ln\left(\frac{v_1}{v_0}\right)} \quad (8)$$

Figure 4a), Fig. 5a) and Fig. 6a) show the calculated average flow stresses σ_f and Fig. 4b), Fig. 5b) and Fig. 6b) show the corresponding forming zone length l_0 for the tested

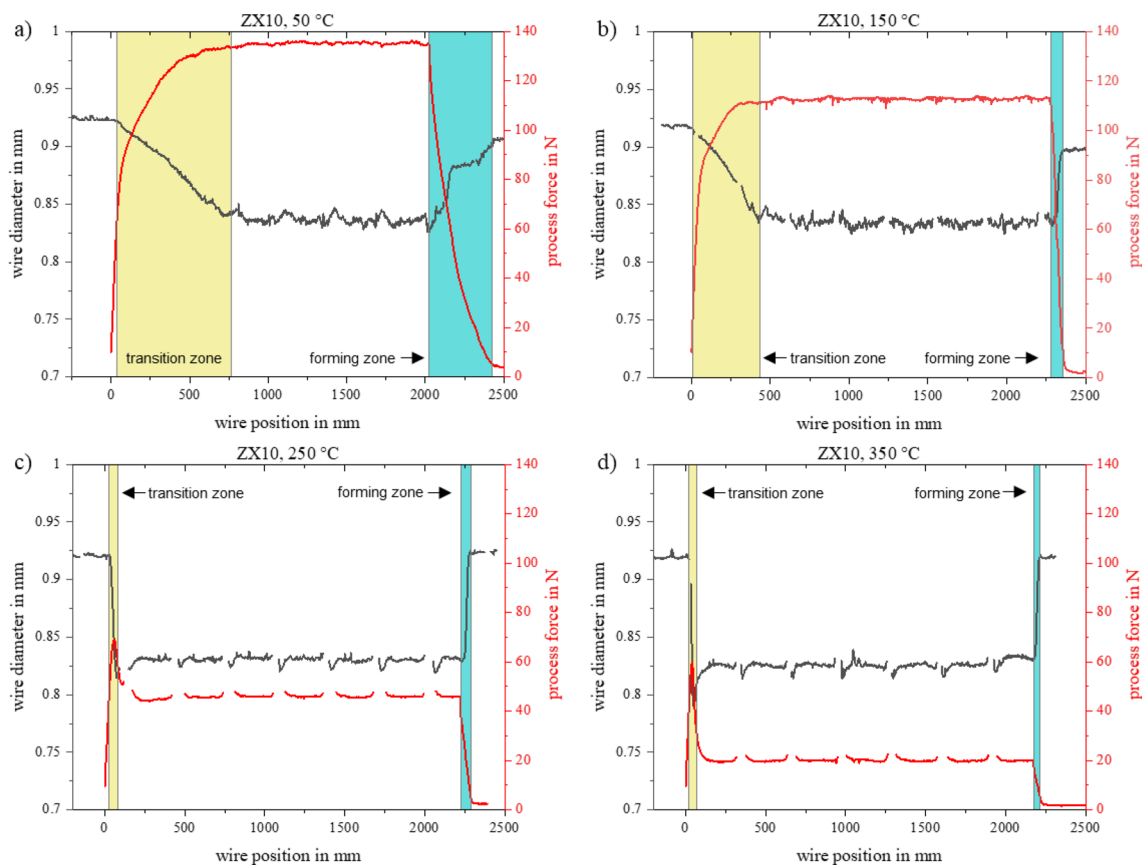


Fig. 3 Representative ZX10 wire diameter and process force evolution at $v_0 = 10$ mm/s and different temperatures

temperature and speed ratio at the chosen feeding speeds for Z1, ZX10 and ZnCu, respectively. The graphs show the flow stresses (figure parts a) and the forming zone lengths (figure parts b) as contour plots for the process temperature versus the speed ratio v_1/v_0 (representative of the CSA reduction). The value of the z-axis (flow stress or forming zone length) is shown in colour and the dots in all graphs represent the respective measurement values of the experiments with the corresponding parameter settings. The contour lines are then created by linear interpolation between two neighbouring measurement points. The grey areas represent process settings for which no information could be extracted due to material failure. Thus, for all Figs. 4, 5 and 6 the grey areas represent non-feasible parameter settings with wire fractures. The evaluation of the graphs for the flow stress and the forming zone length in order to make a statement on the feasibility of the process setting and the definition of the process window can therefore only be carried out for the coloured inner areas and the measuring points themselves, but not for the areas marked in grey.

While analysing the results, it became evident that the analytically and experimentally determined CSA reductions R_{an} and R_{exp} differ from each other. A variation of the two reduction values can be directly related to a disturbance of

the assumed volume constancy (in Eq. 2), translated into a violation of the established steady-state condition of the process, which consists, for example in the non-localisation of the material flow in the forming zone. For general statistical confidence intervals, a widely accepted error is 5% and an allowable margin of error is 10% deviation from the norm [51]. Comparing the parameter settings with CSA reductions of up to 10% allowable deviation in A_1 with the measured forming zone length l_0 , $R_{an} \approx R_{exp}$ occurred at the same parameter settings where the forming zone length is under 100 mm long. Long(er) forming zone lengths imply that the deformation of the wire is distributed over long wire lengths and not localized anymore. In the DD setup used, the distance from the feeding spool to the drawing spool, representing the free wire length, is approx. 745 mm long. Because the highest reduction accuracies are obtained in experiments with forming zone lengths less than 100 mm and the temperature influenced length in the wire is approx. 100–200 mm long [1], a measured forming zone length l_0 greater than 200 mm cannot result in a localized deformation as it exceeds the temperature induced length. Therefore, the feasible process setting ranges in Fig. 4b), Fig. 5b) and Fig. 6b) are evaluated by the forming zone length: short forming zone lengths of less than 100 mm mark

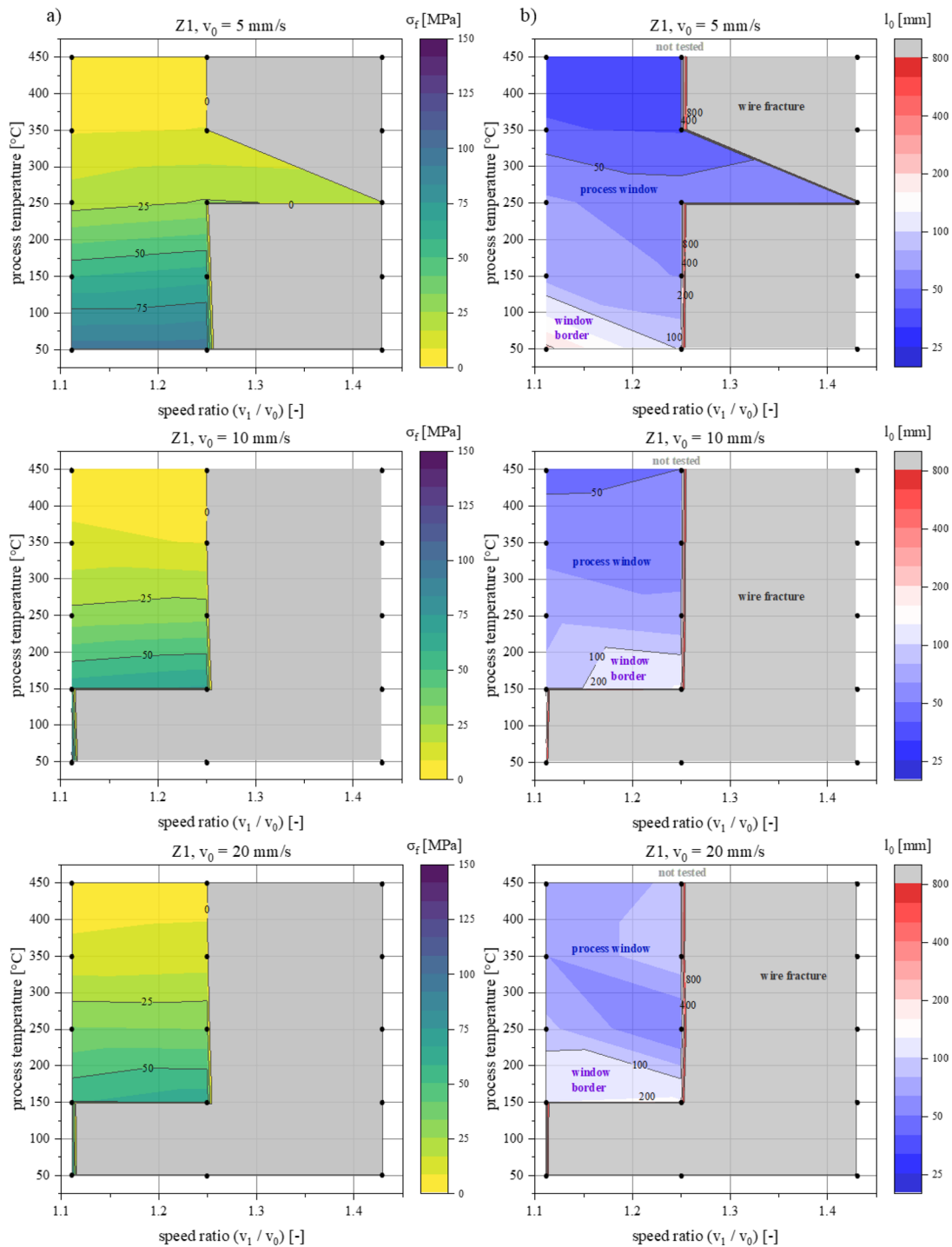


Fig. 4 a) average flow stress and b) forming zone length for Z1

the process window (blue area), forming zone lengths of $100 < l_0 \leq 200$ mm (light area) mark an area of transition at the process window border, and long forming zone lengths over 200 mm (red area) mark the feasible but not localized forming parameter settings.

Figure 4 shows the plots for the Z1 wires. The flow stresses (Fig. 4a) are lower at higher temperatures, as expected from

temperature induced material behaviour. At same temperature levels but with increasing CSA reduction, the tensile stresses are nearly the same when the wire does not fracture. The developed steady-state, which is sensitive to temperature, flow stress and tensile force, appears to be mainly influenced by the temperature, which affects the resulting tensile force in the process. Apart from a few differences at

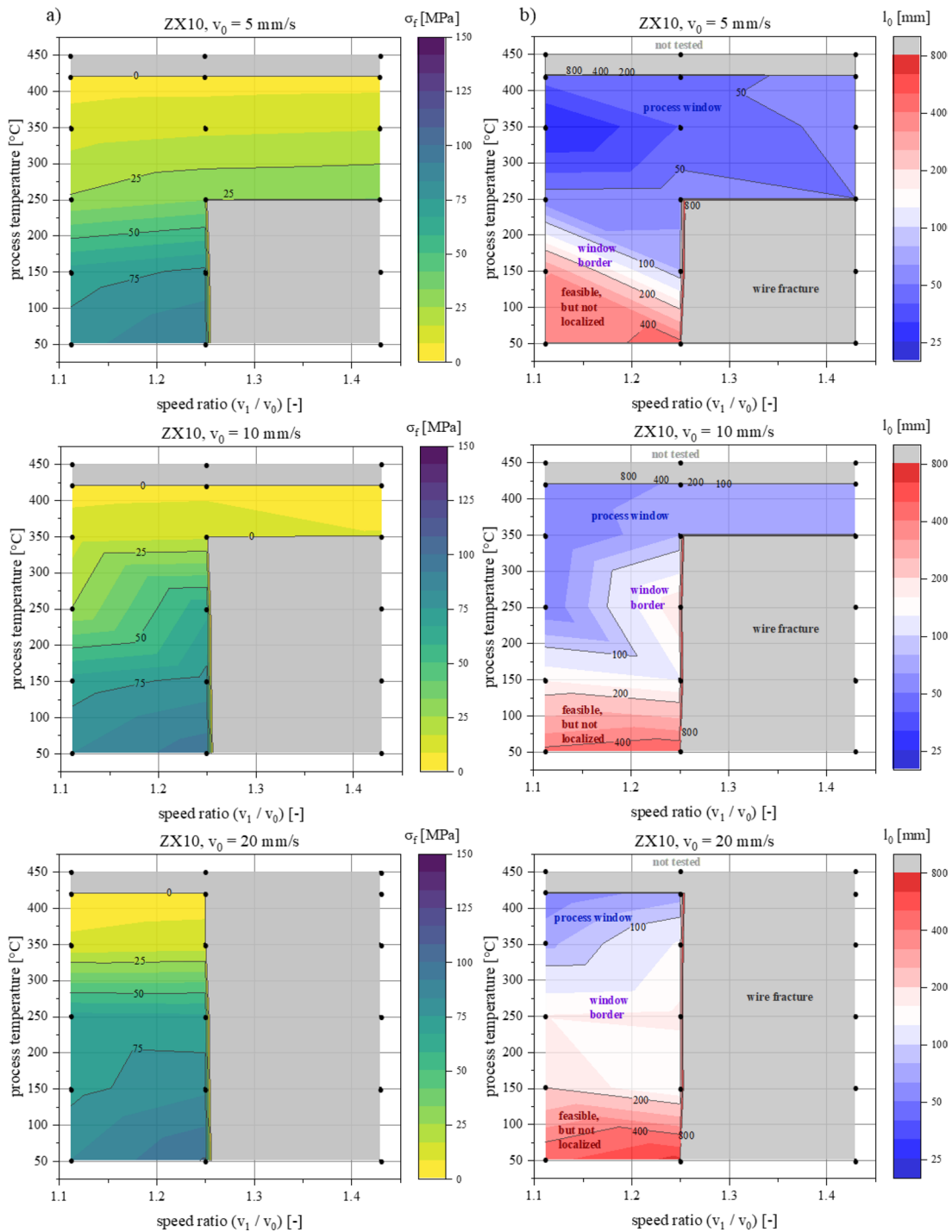


Fig. 5 a) average flow stress and b) forming zone length for ZX10

a feeding speed of 5 mm/s, the basic plot shapes for each feeding speed are similar. At 10 and 20 mm/s feeding speed, experiments at low temperatures of 50 °C are only possible at 10% CSA reduction with high tensile forces. For temperatures of 150 °C and higher, 20% CSA reduction is possible and for temperatures over 250 °C, the flow stress seems to reach an overall minimum. There appears to be little or no

further temperature effect at high temperatures of approx. 300 °C and above. This effect is related to the occurrence of dynamic recrystallisation, which leads to a significant softening of the material [52]. At 5 mm/s feeding speed, CSA reductions of 20% are feasible for all tested temperatures and 30% CSA reduction are feasible at 250 °C. At this lower feeding speed, the temperature effect disappears above

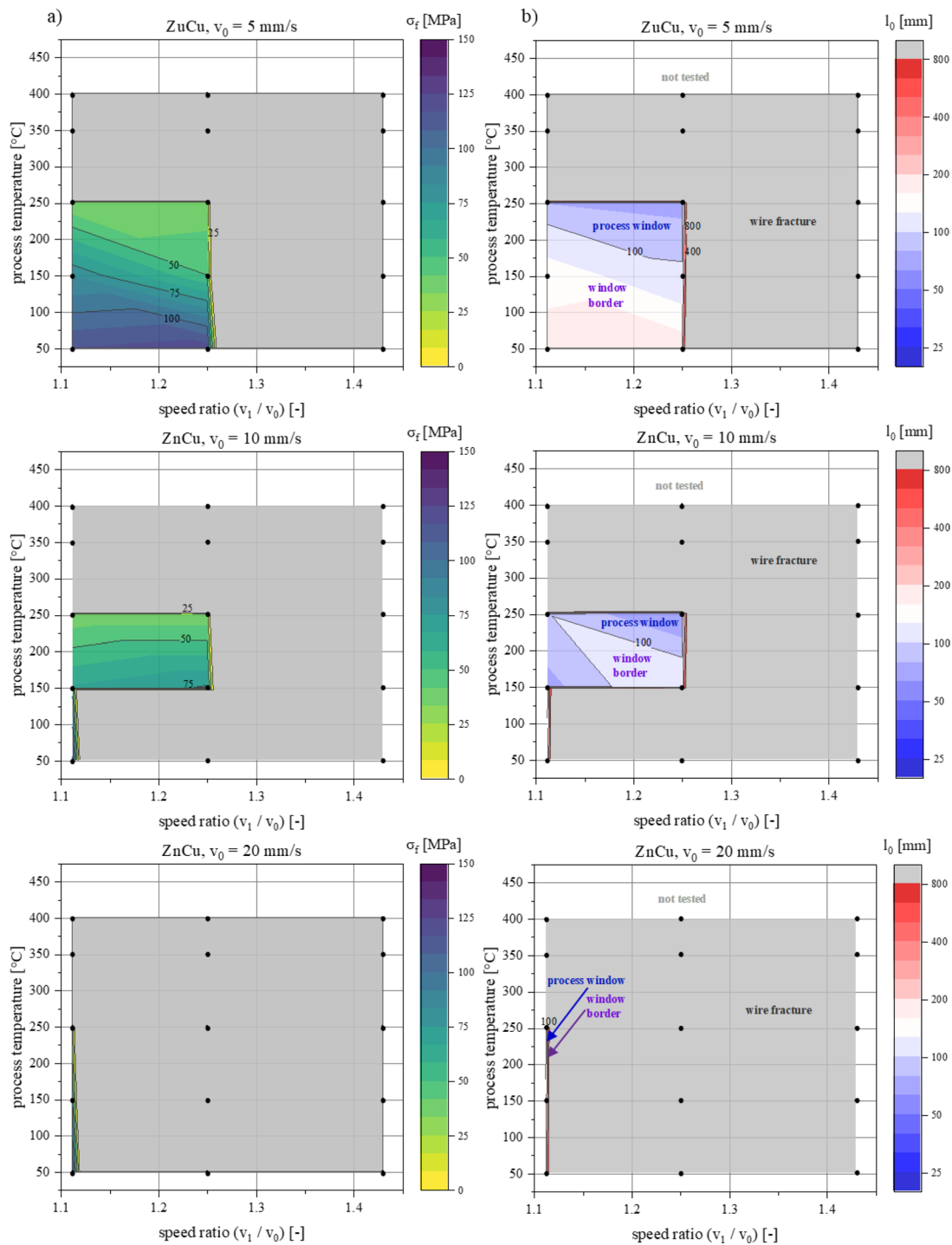
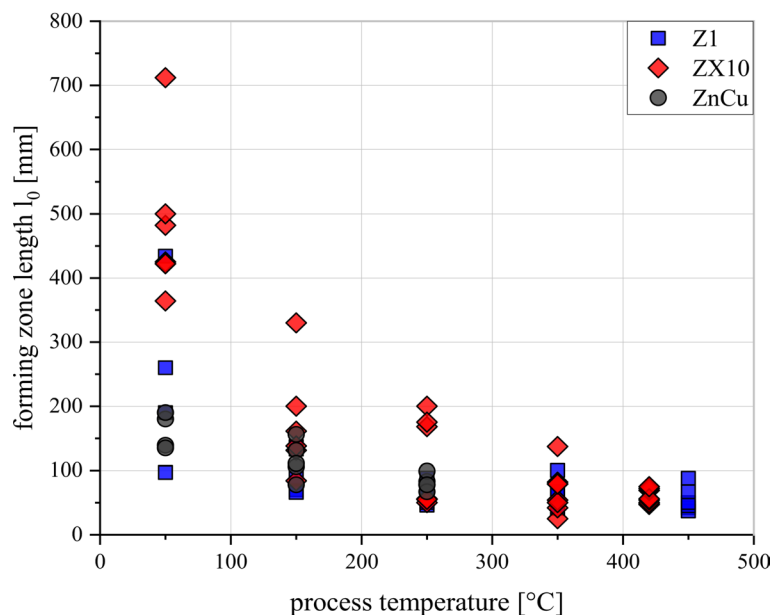


Fig. 6 a) average flow stress and b) forming zone length for ZnCu

250 °C again. In both 5 mm/s plots it can be seen that all set reductions up to and including 20% CSA reduction are possible. In the experiments with 30% CSA reduction, only the experiment at 250 °C is possible. At higher temperatures the material experiences hot cracks and at lower temperatures cold cracks: At lower temperatures, cold failure of the material occurs due to its brittleness and at higher temperatures

the process no longer works due to the speed of thinning when the material is over softened by the induced heat. Both cases are identified as wire fracture (grey areas), as it is not possible for all feeding speeds to make this precise distinction between wire fracture due to the temperature being too high or too low at the set process speeds (e.g. plots at 10 and 20 mm/s feeding speed).

Fig. 7 Forming zone length versus temperature for all experiments



The forming zone contour plot (see Fig. 4b) shapes are similar to the flow stress plots for each feeding speed. Lower flow stresses and shorter forming zones are obtained at the same process parameter settings. Short forming zones (blue areas) are mostly obtained above 150 °C and for up to 20% CSA reduction. Except for a feeding speed of 5 mm/s where the process window is broader, tolerating temperatures of 50 °C at 20% CSA reduction and allowing 30% CSA reduction at 250 °C. At 5 mm/s feeding speed, the wire stays longer in the induction coil generated heating zone, allowing improved through-heating and thus a broader process window with shorter forming zones. This also allows higher strain rates as 30% CSA reduction, but only at 250 °C. At higher temperatures, the material seems to be too soft and at lower temperatures too brittle for these high strain rates. At 50 °C, 10% CSA reduction result in a long forming zone of more than 400 mm. The lack of temperature lets the force increase (see Fig. 3) until a steady-state is reached, which does not allow a localization of the deformation, resulting in long forming zones and inaccurate CSA reduction. Increasing the strain rate at 50 °C to 20% CSA reduction leads to a significantly shorter forming zone of 97 mm. The higher strain rate associated with the 20% CSA reduction results in faster and more intense plastic deformation, leading to greater work hardening and potentially altered thermal effects, ultimately resulting in a significantly shorter forming zone length compared to the 10% CSA reduction process settings. Further increased strain rates then lead to material failure. Increasing the feeding speed will move the wire through the induction coil more quickly. This could affect the efficiency of heat transfer from the induction coil to the wire, potentially resulting in less uniform heating

along the length of the wire and variations in temperature distribution. Changing the feeding speed can affect the rate of plastic deformation experienced by the wire during DD. A higher feeding speed may result in more rapid deformation, potentially affecting the length of the forming zone and the overall process dynamics. Changes to the feed rate can also affect the cooling rate and thus influence the material behaviour and formability after the induction heating zone. This can result in smaller process windows and longer forming zone length with increasing feeding speeds as seen in the 10 and 20 mm/s feeding speed plots.

Overall, shorter forming zones are measured at parameter settings which are achieved in DD experiments carried out at elevated temperatures. Because of the low cold workability of pure Mg, many Mg alloys are hot-worked with reductions of 10–20% [53]. Adding alloying elements such as Zn can not only improve mechanical properties such as yield strength, tensile strength and hardness [54], but also the workability. As Zn can act as a grain refiner, the finer grains can enhance the formability of the material by reducing the likelihood of crack initiation and propagation during deformation processes. It can also increase the ductility of the Mg-alloy, making it more capable of undergoing plastic deformation without fracture, leading to improved formability. Here, elevated process temperatures and adding 1 wt% Zn content make it possible to achieve CSA reductions of up to 30% in a single pass DD experiment.

For ZX10, the plots show larger differences for each feeding speeds. In the flow stress plots (see Fig. 5a), similar tendencies as for the Z1 plots are visible. The stresses are smaller the higher the temperatures. Again, the plots show a region of little or no resolvable temperature effect for

300–420 °C at 5 mm/s and approx. 325–420 °C for higher feeding speeds. The alloying elements seem to delay the dynamic recrystallisation in ZX10. For lower temperatures, increasing the CSA reduction can lead to higher flow stresses this time. While the flow stress of Z1 may remain relatively constant with increasing CSA reduction at the same temperature levels, the presence of Zn and Ca in ZX10 could result in a more pronounced temperature dependence of flow stress for temperatures below 300 °C, leading to variations in flow stress with changing CSA reduction. In both the 5 and 10 mm/s feeding speed plots it can be seen that all CSA reductions up to and including 20% are possible. For the 30% CSA reduction experiments, experiment from 250 (350 for 10 mm/s) to 420 °C are possible. Here again, a distinction is possible between cold failure of the material due to its brittleness and excessively softened material at high temperatures, which can no longer withstand the process forces.

Differences are also seen in the forming zone contour plots for ZX10 (see Fig. 5b). At the lowest feeding speed, the DD experiments between 200 and 420 °C have the shortest forming zones (blue area). All set reductions in CSA enable feasible processing above 200 °C and with good CSA reduction accuracy within temperature ranges of 250–420 °C. At a feeding speed of 10 mm/s, the process window for up to 20% CSA reduction is between 200 and 420 °C and for up to 30% CSA reduction, the process window is between 350 and 420 °C. For the highest feeding speed, that region shrinks to a speed ratio of 1.15–1.25 at about 400 °C only. Reductions in CSA of 30% are no longer possible at 20 mm/s. Compared to the Z1 plots, 30% CSA reduction is possible not only for DD experiments at 5 mm/s feeding speed, but also at 10 mm/s feeding speed and within larger temperature ranges than for Z1. Thus, the addition of less than 1 wt% Ca to the binary Mg-Zn alloy wires, which have a higher formability, allows more robust processing at higher feed rates in this case, as also shown by Chino et al. [55] in their work. Zn contributes to solid solution strengthening and may affect precipitation behaviour, while Ca can refine the grain structure and influence the formation of intermetallic phases. The different effects of these alloying elements on the material properties can lead to variations in the deformation behaviour and process window ranges. The addition of Ca tends to lead to a more brittle failure of the material. As Ca simultaneously influences the development of the microstructure (grain refinement) and leads to a much weaker texture formation due to recrystallisation [56], this embrittlement is compensated by the changed microstructure and processing may only be possible at the right combination of temperature and strain rate [57]. This effect is visible in Fig. 5b by smaller process windows with increasing

feeding speeds and forming zones below 100 mm mostly occurring at temperatures above 250 °C.

For ZnCu (see Fig. 6), the process window is more localized at smaller process parameter ranges than for the Mg-alloys. The values in the tensile stress plots (see Fig. 6a) are generally higher, which indicates a lower temperature response of the Zn-material, resulting in lower material flow stresses. In the case of the ZnCu wires, increasing the temperature will soften the material and therefore reduce its yield stress, but will not necessarily increase the possible diameter reductions. On the other hand, increasing the feeding speed significantly reduces the range of possible process parameter settings. Even though ZnCu alloys can also show superplastic behaviour with elongations of up to 470% [58], the tested Zn wires did not reach 30% CSA reduction – mostly not even 20%. Similar material effect occurred in DD experiments in earlier work [1]. This could be due to its low melting point of around 420 °C [59] in combination with a recrystallisation temperature at room temperature [60], leading to non-activation of superplasticity [61]. Superplastic behaviour can occur at elevated temperatures, typically 0.5–0.7 times the melting point, where the material exhibits high ductility and low flow stress. For ZnCu, which has a melting point of approximately 420 °C, the temperature range for superplastic behaviour would be roughly 210–294 °C. However, even though these temperatures are reached, the ZnCu wires do not show superplastic behaviour in the DD experiments. Superplasticity is a mechanism involving grain boundary sliding, which does not occur at high strain rates and may explain the small diameter reductions achieved for the ZnCu wires. According to the measurements, we see a high strain rate sensitivity in the alloy. Supporting this, Bednarczyk et al. [62] show in their study that Zn deformation responses vary significantly at different strain rate conditions. Altogether, the Zn-material appears to have a lower temperature response while conjecturing a more limited strain rate sensitivity than the used Mg-materials.

In Fig. 6b) in the forming zone length plots, the process window region with short l_0 is concentrated around 200–250 °C at maximum 20% CSA reduction and feeding speeds of maximum 10 mm/s. Experiments with temperatures over 250 °C are not possible. Looking at the length of the forming zones and the process windows, there is a strong strain rate sensitivity of the ZnCu material visible. Increasing the feeding speed or the speed ratio often leads directly to wire fracture. In general, the forming zones in the ZnCu experiments are longer than for the Mg wires tested. While the ZnCu wires are more capable of accommodating plastic deformation through mechanisms such as grain boundary or dislocation sliding, they may exhibit more homogeneous and less localized deformation compared to the Mg wires.

In addition, differences in temperature sensitivity between the tested materials may influence the extent of deformation localization under the same process settings. Again, the length of the measured forming zone correlates with the accuracy of the achieved CSA reduction and therefore influences the quality of the process.

For all tested materials in general, the flow stress of the material is significantly reduced at higher temperatures, making it easier to localize deforming. The rather low flow stresses within the feasible processing range indicate active dynamic recrystallisation / recovery. This means that the recrystallisation temperature of the respective materials lies in between the process temperatures investigated, and a stable onset of the desired dynamic recrystallisation can be associated with stable process control. Furthermore, the longer the forming zone l_0 , the more likely it is that reduction inaccuracies will occur, which equates to a violation of the established steady-state condition of the process. In these cases, (Eq. 2) and thus (Eq. 5) do not apply anymore, because a localization of the forming is not happening. For all parameter settings it is evident that the length of the forming zone has an influence on the achieved reductions being close to the set reductions and thus on the process quality. And it appears that the areas with forming zone lengths of up to 75 mm have significant localization to coincide with good CSA reduction accuracy of up to 10% tolerance. However, as no such measurements were observed, too small forming zone lengths of less than 25 mm could be unfavourable, too.

Figure 7 shows the measured forming zone lengths for the used temperatures. All materials show short forming zones up to approx. 100 mm length for temperatures over 250 °C. Except for the ZnCu alloy, which shows forming zone lengths around 100 mm with no big deviations for 250 °C but had no feasible parameter settings for temperatures over 250 °C. Forming zone length over 100 mm are measured for experiments done at low temperatures. For temperatures of 150 °C and lower, the forming zone lengths vary more for all used materials, especially for the Mg alloys. This affirms the prior statement that long forming zones and less stable process settings go along while too short forming zones could lead to wire fracture as no forming zone length less than 25 mm is measured. Because the temperature is the main influencing process parameter, the process quality is influenced by the process temperature, reconfirming prior results. There is a clear trend towards more localized deformation with increasing temperature. Higher temperatures lead to higher gradients in material flow stress over the wire's length, resulting in more localized forming. This way the tensile load is concentrated on local CSA reduction instead of (elastic) forming of longer wire parts.

Mechanical properties of the drawn wires

For an application as biodegradable wires, not only the feasibility of the DD process and a known process window are important, but also the resulting mechanical properties. Figures 8, 9 and 10 show the tensile yield stress (TYS) in blue, the ultimate tensile stress (UTS) in grey and the fracture strain in red for all produced DD wires for Z1, ZX10 and ZnCu, respectively. The different set CSA reductions are represented by empty, half-empty and full squares for all experiments. Additionally in each graph, the green filled triangles show the values for the as-extruded wires for better comparison with the DD wires.

For Z1 (see Fig. 8), there are tendencies of decreasing resulting TYS and UTS at increasing process temperatures. For all feeding speeds, the UTS of the as-extruded wires can be recreated, while the TYS is always lower. The fracture strain is similar to the as-extruded wires for process temperatures of over 250 °C. At lower temperatures, the fracture strain decreases and in combination with slightly higher TYS and UTS, cold-forming effects occur. There appear to be no significant changes in the mechanical properties for different feeding speeds and different set CSA reductions for Z1. A similar effect can be seen in Fig. 4 for the flow stress and the forming zone length. Process temperatures of 250 and 350 °C can recreate the as-extruded wire properties. However, higher temperatures result in decreasing UTS, TYS and fracture strain. Here, work softening effects resulting from elevated temperature can persist in the Z1 wires even after cooling to room temperature. The reduced strength and ductility associated with material softening can lead to lower UTS, TYS, and fracture strain values in the Z1 wires.

In Fig. 4, the process window for Z1 is for 5 mm/s feeding speed between 150 and 450 °C at 10 and 20% CSA reduction and at 250 °C for 30% CSA reduction. For 10 mm/s it is between 150 and 450 °C for 10 and 20% CSA reduction. At 20 mm/s, the process window is between 350 and 450 °C for 10% CSA reduction and between 150 and 450 °C for 20% CSA reduction. When comparing the associated parameter settings with the mechanical properties of the wires, there is no strong correlation, except for the tendency to have mechanical properties close to those of the extruded wires. Focussing on short forming zones of under 50 mm length only, mostly the wires produced at 150 and 450 °C fall out of the mentioned areas, leaving the process settings resulting in wires with mechanical properties similar to the extruded wires.

For ZX10 (see Fig. 9) different mechanical properties are measured for different feeding speeds and CSA reductions. A general tendency of lower TYS and UTS at higher process temperatures and cold-forming effects at lower process temperatures is visible again. Contrary to this, the fracture strain seems to increase with increasing process

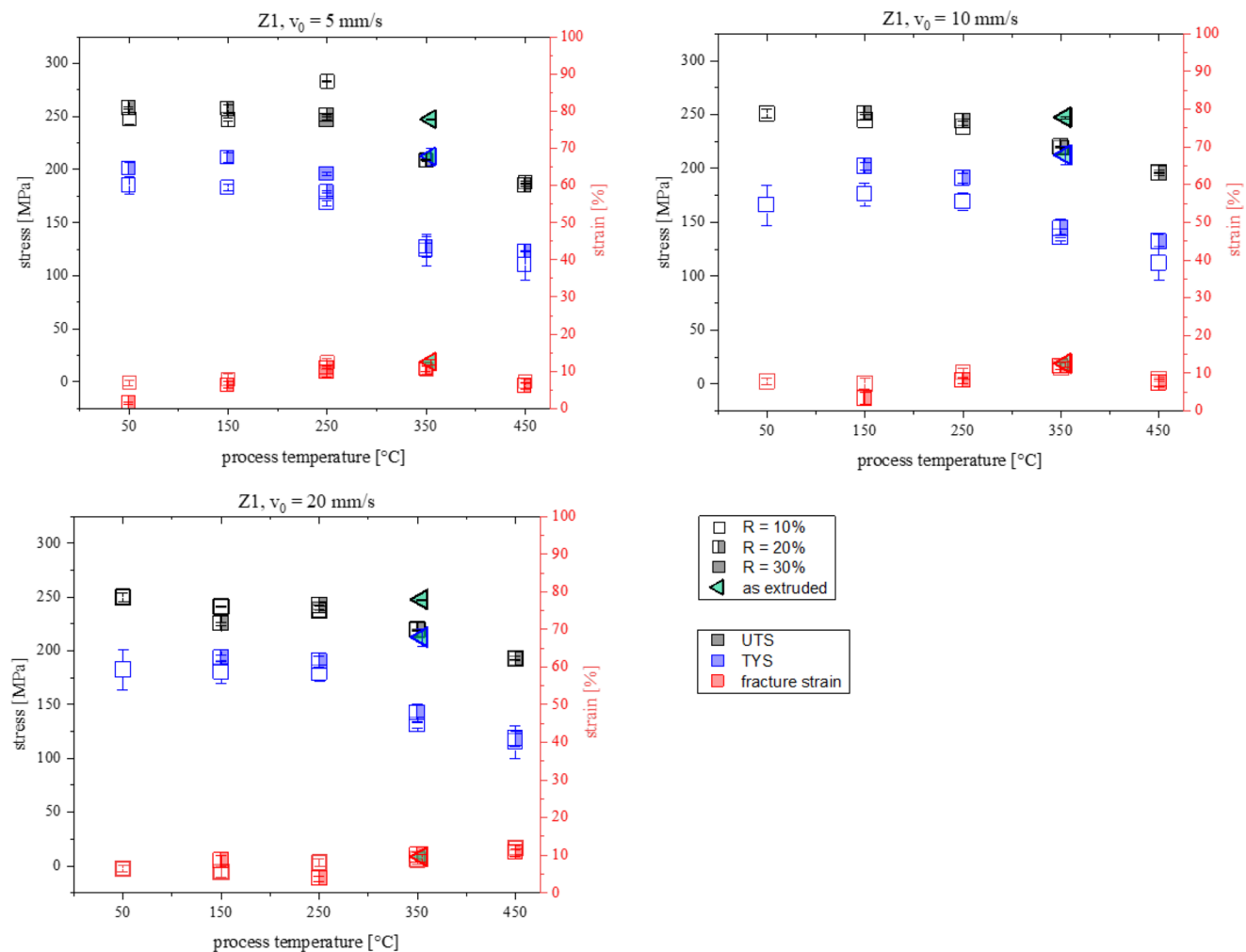


Fig. 8 Mechanical properties for Z1 wires

temperatures, especially for 20% CSA reduction. For TYS significantly and for UTS slightly, higher values are measured with increasing CSA reductions at all feeding speeds, while for the fracture strain, the effect is the opposite with lower values with increasing CSA reductions. Higher CSA reductions typically result in greater plastic deformation and strain accumulation within the material during DD. This increased plastic deformation leads to a higher degree of work hardening which can increase the UTS and TYS of the material due to increased dislocation density and strengthening effects. While higher levels of deformation can improve UTS and TYS through strain hardening and strengthening mechanisms, they can also promote the formation of microstructural defects or crack nucleation sites, resulting in lower fracture strain values. For feeding speeds of 10 and 20 mm/s, the mechanical properties of the DD and as-extruded wires are similar at process temperatures of 350 and 450 °C. For 5 mm/s feeding speed, the fracture strain is similar, but the TYS

and UTS differ. Again, mechanical properties of the as-extruded wires can be recreated. ZX10 wires that exceed lower CSA reductions will result in higher elongation at break but lower TYS.

Compared to the Z1 wires, the ZX10 alloy has a higher sensitivity to strain rates and process settings as seen in Fig. 5. In Fig. 5, the process window with forming zones of less than 50 mm lengths is for 5 mm/s feeding speed between approx. 275 and 375 °C for 10 and 20% CSA reduction and between at 250 °C for 30% CSA reduction. For 10 mm/s, the area is between 350 and 420 °C for all set CSA reductions and for 20 mm/s between 350 and 450 °C only for 10 and 20% CSA reductions. Comparing these areas and their related process setting with the mechanical properties of the wires again, there seems to be a correlation short forming zones and mechanical properties close to the as-extruded wires. As the resulting mechanical properties of the Mg-alloys vary depending on different process settings, property customisation can be possible by applying the DD process.

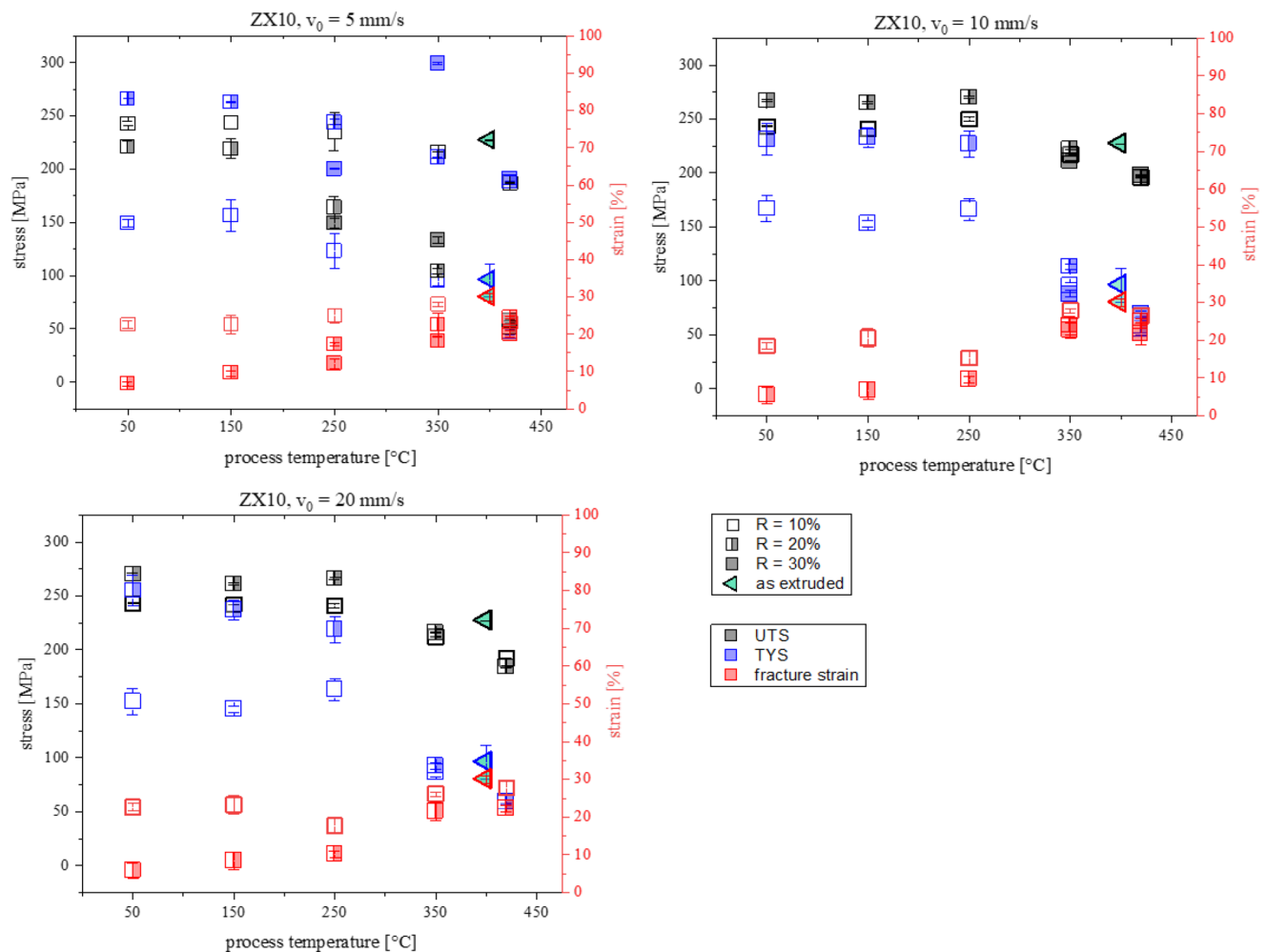


Fig. 9 Mechanical properties for ZX10 wires

The mechanical properties of the ZnCu wires (see Fig. 10) and the as-extruded wires do not differ significantly for all process settings or rather are within the range of values. The only exception is a more than doubled fracture strain for DD wires produced at 150 °C and 5 mm/s feeding speed with a set CSA reduction of 20%. These specific process settings may represent an optimal combination that enhances ductility and fracture strain in the wires due to the strain rate sensitivity of the material. Thus, the combination of moderate temperature and moderate strain rate during DD may promote the higher fracture strain in the ZnCu wires. In addition, the fracture strain values show significantly higher deviations compared to the YTS and UTS values. This may indicate inhomogeneous wires.

In contrast to the Mg-alloys, the ZnCu wires do not show cold-forming effects at low process temperatures. Additionally, the low recrystallization temperature results in similar mechanical properties for all process parameter settings. As the mechanical properties do not differ much from the

as-extruded wires, the as-extruded properties can be recreated, but property customisation could be less effective compared to the Mg wires. Except perhaps in the one case at 5 mm/s feeding speed where the used parameter settings result in a doubled elongation at break of the wire. In Fig. 6, the process window for ZnCu for 5 mm/s feeding speed is between 200 and 250 °C for 10 and 20% CSA reduction. For 10 mm/s the area is between 200 and 250 °C for 20% CSA reduction and only around 250 °C for 10% CSA reduction. For ZnCu, a correlation between short forming zone lengths and resulting mechanical properties similar to the as-extruded condition is not as distinct as for the Mg materials.

Summary and conclusions

The aim of this work was to develop and evaluate process windows for Mg- and Zn-based wires and to discuss the resulting wire properties. To achieve this, dieless wire

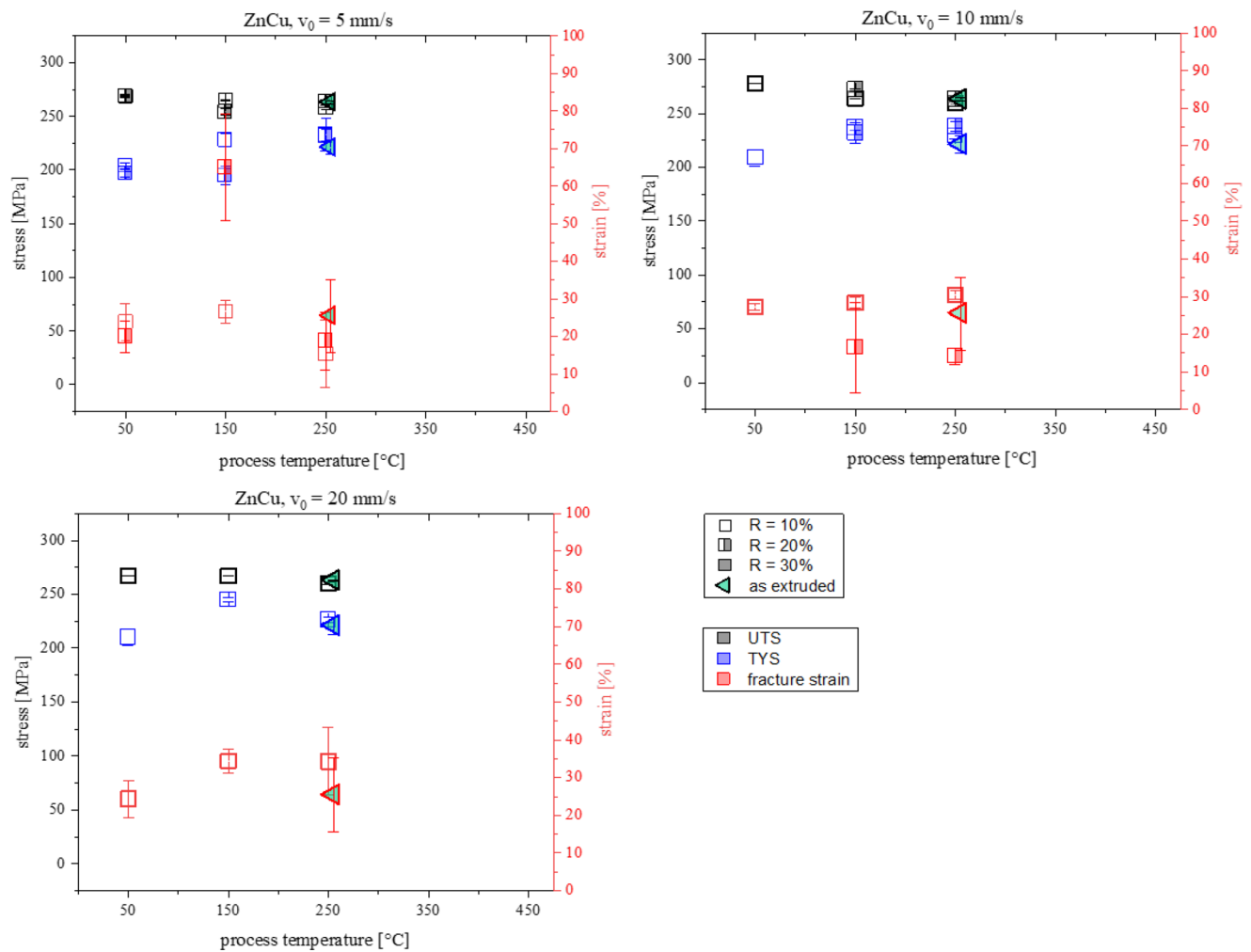


Fig. 10 Mechanical properties for ZnCu wires

drawing experiments at different process temperatures and speeds were carried out using directly extruded Z1, ZX10 and ZnCu wires. The process parameters and their resulting wire diameter evolution and mechanical wire properties were compared and discussed. As emphasized, the length of the forming zone is an important indicator for the process window and the accuracy of chosen parameter settings in the dieless drawing process. As shown above, a short forming zone resulting in localized deformation of the wire is found on wires with accurate diameter results. The results of this work relate to 1 mm thick Mg- and Zn-based wires of selected alloys, but also allow general conclusions to be drawn. For more fundamental conclusions, combined numerical-experimental investigations should be carried out.

During this work, the following main results were obtained:

- The dieless drawing process and its results are clearly material depended.
- CSA reductions of up to 30% are possible for Z1 and ZX10 in one wire drawing step.
- The dieless drawing process and its results are primarily influenced by the process temperature and secondarily by the feeding speed and the set CSA reduction.
- Obtained process windows can be evaluated by the forming zone length as an indication of process quality.
- Highest possible CSA reduction is achieved with process parameter settings that result in the best localization of the deformation.
- The best localization of the forming of the wire occurs with short forming zone lengths between 25 and 75 mm at high temperatures of 250 °C and above.
- Different parameter settings result in different mechanical properties of the wires.
- Dieless drawing process temperatures close to the wire extrusion temperature result in mechanical properties similar to the as-extruded wires.

Acknowledgements The authors would like to thank Dr. Maria Nienaber for her help with the extrusion of the wires and Ms. Alexia Gurgadse for carrying out part of the tensile tests.

Author contributions All authors contributed to the study conception and design. Material preparation, data collection and analysis were performed by Merle Braatz. The first draft of the manuscript was written by Merle Braatz and all authors commented on previous versions of the manuscript. All authors read and approved the final manuscript.

Funding Open Access funding enabled and organized by Projekt DEAL.

Declarations

Conflict of interest The authors declare that they have no conflict of interest. This research did not receive any specific grant from funding agencies in the public, commercial or non-profit sectors other than the general funding of the Helmholtz Zentrum Hereon.

Open Access This article is licensed under a Creative Commons Attribution 4.0 International License, which permits use, sharing, adaptation, distribution and reproduction in any medium or format, as long as you give appropriate credit to the original author(s) and the source, provide a link to the Creative Commons licence, and indicate if changes were made. The images or other third party material in this article are included in the article's Creative Commons licence, unless indicated otherwise in a credit line to the material. If material is not included in the article's Creative Commons licence and your intended use is not permitted by statutory regulation or exceeds the permitted use, you will need to obtain permission directly from the copyright holder. To view a copy of this licence, visit <http://creativecommons.org/licenses/by/4.0/>.

References

- Braatz M, Bohlen J, Ben Khalifa N (2024) Experimental and Numerical Investigation of the Forming Zone in Dieless Wire Drawing Process of Thin Biometallic Wires, in Proceedings of the 14th International Conference on the Technology of Plasticity - Current Trends in the Technology of Plasticity. pp. 479–490. https://doi.org/10.1007/978-3-031-41023-9_49
- Tiernan P, Hillery MT (2008) An analysis of wire manufacture using the dieless drawing method. *J Manuf Process* 10(1):12–20. <https://doi.org/10.1016/j.manpro.2008.05.001>
- Weiss V, Kot RA (1969) Die-less wire drawing with transformation plasticity. *Wire J* 2(9):182–189
- Sekiguchi H, Kobatake K (1977) An analysis of temperature distribution in continuous dieless drawing. *Nara Natl Coll Technol Res Bull* 13:47–53
- Naughton MD, Tiernan P (2007) Requirements of a dieless wire drawing system. *J Mater Process Technol* 191(1–3):310–313. <https://doi.org/10.1016/j.jmatprotec.2007.03.054>
- Dodyim N et al (2020) Drawing of magnesium fine wire and medical application of drawn wire. *Procedia Manuf* 50:271–275. <https://doi.org/10.1016/j.promfg.2020.08.050>
- Ohno A et al (1982) New Tapered-Rod forming process for Coil Springs. *SAE Tech Paper* 820130:471–478. <https://doi.org/10.4271/820130>
- Hongyu W et al (2018) Analysis and study of dieless drawing process for rod based on radial direction gradient slab method. *Int J Adv Manuf Technol* 98(1–4):839–847. <https://doi.org/10.1007/s00170-018-2282-5>
- Seitz J-M et al (2011) The manufacture of Resorbable suture material from Magnesium - drawing and stranding of thin wires. *Adv Eng Mater* 13(12):1087–1095. <https://doi.org/10.1002/adem.201100152>
- Tiernan P, Hillery MT (2004) Dieless wire drawing - an experimental and numerical analysis. *J Mater Process Technol* 155:1178–1183. <https://doi.org/10.1016/j.jmatprotec.2004.04.175>
- Furushima T, Hirose S, Manabe K-i (2009) Effective temperature distribution and drawing speed control for stable Dieless drawing process of metal tubes. *J Solid Mech Mater Eng* 3(2):236–246. <https://doi.org/10.1299/jmmp.3.236>
- Milenin A et al (2018) Computer aided design of the laser dieless drawing process of tubes from magnesium alloy with take into account ductility of the material. *Proc 17th Int Conf Metal Form Metal Form 2018* 15:302–310. <https://doi.org/10.1016/j.promfg.2018.07.223>
- Furushima T, Manabe K (2009) Finite element Simulation with coupled Thermo-Mechanical analysis of Superplastic Dieless Tube drawing considering strain rate sensitivity. *Mater Trans* 50(1):161–166. <https://doi.org/10.2320/matertrans.P-MRA2008837>
- Milenin A et al (2014) Computer aided design of Wires Extrusion from biocompatible Mg-Ca Magnesium Alloy. *Arch Metall Mater* 59(2):551–556. <https://doi.org/10.2478/amm-2014-0091>
- Furushima T, Manabe K (2007) Experimental and numerical study on deformation behavior in dieless drawing process of superplastic microtubes. *J Mater Process Technol* 191(1–3):59–63. <https://doi.org/10.1016/j.jmatprotec.2007.03.084>
- Fortunier R, Sassoulas H, Montheillet F (1997) A thermo-mechanical analysis of stability in dieless wire drawing. *Int J Mech Sci* 39(5):615–627. [https://doi.org/10.1016/s0020-7403\(96\)00060-4](https://doi.org/10.1016/s0020-7403(96)00060-4)
- Pawelski O, Kolling A (1995) Calculation of the temperature distribution in dieless drawing. *Steel Res* 66(2):50–54. <https://doi.org/10.1002/srin.199501087>
- Weidig U, Steinhoff K (2008) Neue Perspektiven und Anwendungen für das frei Längen, in *Umformtechnik im Spannungsfeld zwischen Plastomechanik und Werkstofftechnik*, K. Steinhoff and R. Knopp, Editors. Grips media GmbH: Bad Harburg. pp. 217–231
- Wengenroth W, Pawelski O, Rasp W (2001) Theoretical and experimental investigations into dieless drawing. *Steel Res* 72(10):402–405. <https://doi.org/10.1002/srin.200100141>
- He Y et al (2011) Processing limit maps for the stable deformation of dieless drawing. *Int J Minerals Metall Mater* 18(3):330–337. <https://doi.org/10.1007/s12613-011-0443-8>
- Hwang Y-M, Liu H-H, Wang Y-T (2022) Investigations of Formability and Dynamic Recrystallization Development of Titanium alloys during Dieless Wire drawing processes. *Steel Res Int* 94(2). <https://doi.org/10.1002/srin.202200113>
- von Eynatten K, Reissner JN (2004) Dieless Drawing for Flexible Processing of Microstructure and Mechanical Properties, in *Proceedings of the 34th International MATADOR Conference*, S. Hinduja, Editor. Springer: London. pp. 187–192. https://doi.org/10.1007/978-1-4471-0647-0_28
- Braatz M, Bohlen J, Ben Khalifa N (2022) Process Stability and Reproducibility of the Dieless drawing process for AZ31 magnesium wires. *Key Eng Mater* 926:389–400. <https://doi.org/10.4028/p-lm7s8y>
- Kustra P et al (2023) Novel drawing technology for high area reduction manufacturing of ultra-thin brass wires. *Archives Civil Mech Eng* 23(3). <https://doi.org/10.1007/s43452-023-00677-9>
- Li K (2018) Liu. *Metal Flow Law of Variable Diameter Metal Wire during die drawing*. CMC 2017. Springer, Singapore. DOI. https://doi.org/10.1007/978-981-13-0107-0_56

26. Kishimoto T, Du P, Furushima T (2022) Effect of microstructure on outer surface roughening of magnesium alloy tubes in dieless mandrel drawing. *J Magnesium Alloys* 10(10):2730–2744. <https://doi.org/10.1016/j.jma.2022.02.001>
27. Kishimoto T, Furushima T (2023) Achieving thin wall and high surface quality of magnesium alloy tubes in combined process of hollow sinking after die-less mandrel drawing. *Int J Mater Form* 16(3). <https://doi.org/10.1007/s12289-023-01750-7>
28. Milenin A et al (2020) Production of zinc wire for use as a high strength biodegradable surgical threads. *Procedia Manuf* 50:757–760. <https://doi.org/10.1016/j.promfg.2020.08.136>
29. Milenin A et al (2021) Mechanical properties, crystallographic texture, and in vitro bio-corrosion of low-alloyed Zn-Mg, produced by hot and cold drawing for biodegradable surgical wires. *Archives Civil Mech Eng* 21(4). <https://doi.org/10.1007/s43452-021-00311-6>
30. Seitz J-M et al (2010) The manufacture of Resorbable suture material from Magnesium. *Adv Eng Mater* 12(11):1099–1105. <https://doi.org/10.1002/adem.201000191>
31. Mei D et al (2021) Corrosion behavior of mg wires for ureteral stent in artificial urine solution. *Corros Sci* 189:109567. <https://doi.org/10.1016/j.corsci.2021.109567>
32. Champagne S et al (2019) In Vitro Degradation of Absorbable Zinc Alloys in Artificial urine. *Mater (Basel)* 12(2). <https://doi.org/10.3390/ma12020295>
33. Venezuela J, Dargusch MS (2019) The influence of alloying and fabrication techniques on the mechanical properties, biodegradability and biocompatibility of zinc: a comprehensive review. *Acta Biomater* 87:1–40. <https://doi.org/10.1016/j.actbio.2019.01.035>
34. Hirsch J, Al-Samman T (2013) Superior light metals by texture engineering: optimized aluminum and magnesium alloys for automotive applications. *Acta Mater* 61(3):818–843. <https://doi.org/10.1016/j.actamat.2012.10.044>
35. Yoshida K, Koiwa A (2011) Cold drawing of Magnesium Alloy tubes for Medical. *J Solid Mech Mater Eng* 5(12):1071–1078. <https://doi.org/10.1299/jmmp.5.1071>
36. Nienaber M et al (2022) Property profile development during wire extrusion and wire drawing of magnesium alloys AZ31 and ZX10. *Mater Design* 224. <https://doi.org/10.1016/j.matdes.2022.111355>
37. Zander D, Zumdick NA (2015) Influence of ca and zn on the microstructure and corrosion of biodegradable Mg–Ca–Zn alloys. *Corros Sci* 93:222–233. <https://doi.org/10.1016/j.corsci.2015.01.027>
38. Li Z et al (2008) The development of binary Mg–Ca alloys for use as biodegradable materials within bone. *Biomaterials* 29(10):1329–1344. <https://doi.org/10.1016/j.biomaterials.2007.12.021>
39. Meza-García E et al (2015) Influence of alloying elements and extrusion process parameter on the recrystallization process of Mg–Zn alloys. *Mater Today: Proc* 2:S19–S25. <https://doi.org/10.1016/j.matpr.2015.05.004>
40. Li H et al (2016) The influence of Zn Content on the corrosion and wear performance of Mg–Zn–Ca Alloy in simulated body fluid. *J Mater Eng Perform* 25(9):3890–3895. <https://doi.org/10.1007/s11665-016-2207-0>
41. Zhang BP, Wang Y, Geng L (2011) Research on Mg–Zn–Ca Alloy as Degradable Biomaterial, in *Biomaterials—Physics and Chemistry*, R. Pignatello, Editor. In Tech: Zurich. pp. 183–204
42. Bakhsheshi-Rad HR et al (2012) Relationship between the corrosion behavior and the thermal characteristics and microstructure of Mg–0.5Ca–xZn alloys. *Corros Sci* 64:184–197. <https://doi.org/10.1016/j.corsci.2012.07.015>
43. Rad HRB et al (2012) Microstructure analysis and corrosion behavior of biodegradable Mg–Ca implant alloys. *Mater Design* 33:88–97. <https://doi.org/10.1016/j.matdes.2011.06.057>
44. Palai D et al (2022) Influence of copper on the Microstructural, Mechanical, and Biological properties of commercially pure Zn-Based alloys for a potential biodegradable Implant. *ACS Biomaterials Sci Eng* 8(4):1443–1463. <https://doi.org/10.1021/acsbiomaterials.1c01111>
45. Tang Z et al (2017) Potential biodegradable Zn–Cu binary alloys developed for cardiovascular implant applications. *J Mech Behav Biomed Mater* 72:182–191. <https://doi.org/10.1016/j.jmbbm.2017.05.013>
46. Nienaber M et al (2020) On the direct extrusion of Magnesium wires from Mg–Al–Zn Series alloys. *Metals* 10(9). <https://doi.org/10.3390/met10091208>
47. Braatz M et al (2022) Experimental Setup of Dieless Drawing Process for Magnesium Wire, in *Production at the Leading Edge of Technology*. pp. 38–46. https://doi.org/10.1007/978-3-030-78424-9_5
48. Tools K (2023) *Emissivity Chart for Metal Materials*
49. Carolan R, Tiernan P (2009) Computer controlled system for dieless drawing of tool steel bar. *J Mater Process Technol* 209(7):3335–3342. <https://doi.org/10.1016/j.jmatprotec.2008.07.048>
50. Furushima T, Ikeda T, Manabe K (2011) Deformation and Heat Transfer Analysis for high speed Dieless drawing of AZ31 Magnesium Alloy tubes. *Adv Mater Res* 418–420. <https://doi.org/10.4028/www.scientific.net/AMR.418-420.1036>
51. Snedecor GW, Cochran WG (1989) *Statistical methods*, vol 1191, 8 edn. Ames, Iowa Iowa state University, 2
52. Kaibyshev R (2012) Dynamic recrystallization in magnesium alloys, in *advances in wrought magnesium alloys*. Woodhead Publishing 186–225. <https://doi.org/10.1533/9780857093844.1.186>
53. Izumi S (1987) *Non-ferrous metal*. The Japan Institute of Metals, pp 108–109
54. Koç E et al (2015) Influence of zinc on the microstructure, mechanical properties and in vitro corrosion behavior of magnesium–zinc binary alloys. *J Alloys Compd* 648:291–296. <https://doi.org/10.1016/j.jallcom.2015.06.227>
55. Chino Y et al (2011) Effects of ca on Tensile properties and Stretch Formability at Room temperature in Mg–Zn and Mg–Al Alloys. *Mater Trans* 52(7):1477–1482. <https://doi.org/10.2320/matertrans.M2011048>
56. Cano-Castillo G et al (2020) Effect of ca and nd on the microstructural development during dynamic and static recrystallization of indirectly extruded Mg–Zn based alloys. *Mater Sci Engineering: A* 793. <https://doi.org/10.1016/j.msea.2020.139527>
57. Rao KP et al (2018) Review on Hot Working Behavior and Strength of Calcium-Containing Magnesium Alloys. *Adv Eng Mater* 20(9). <https://doi.org/10.1002/adem.201701102>
58. Mostaed E et al (2019) Precipitation induced room temperature superplasticity in Zn–Cu alloys. *Mater Lett* 244:203–206. <https://doi.org/10.1016/j.matlet.2019.02.084>
59. Goodwin FE (2018) *Zinc and Zinc Alloys*. Springer handbook of materials data. Springer, Cham, pp 427–438. DOI: <https://doi.org/10.1007/978-3-319-69743-7.H>. Warlimont and W. Martienssen, Editors
60. Farge JCT (1965) *Recrystallization of zinc alloys*. McGill University: Canada
61. Edington JW (1982) Microstructural aspects of superplasticity. *Metall Trans A* 13(5):703–715. <https://doi.org/10.1007/bf02642384>
62. Bednarczyk W et al (2023) Investigation of slip systems activity and grain boundary sliding in fine-grained superplastic zinc alloy. *Archives Civil Mech Eng* 23(4). <https://doi.org/10.1007/s43452-023-00793-6>

Publisher's Note Springer Nature remains neutral with regard to jurisdictional claims in published maps and institutional affiliations.